ADVANCED PM TECHNOLOGIES TO MANUFACTURE THERMOELECTRIC MATERIALS AND SUPERCAPACITORS

Thomas Weissgaerber, Vicente Pacheco, Carmen Recknagel, Gunnar Walther,

Burghardt Klöden, Bernd Kieback

Fraunhofer-Institute for Manufacturing and Advanced Materials,

Branch Lab Powder Metallurgy and Composite Materials Dresden,

Winterbergstrasse 28, 01277 Dresden, Germany

THERMOELECTRIC MATERIALS

INTRODUCTION

The effective recovery of waste heat will contribute greatly to enhance energy efficiency, to reduce greenhouse gas emission, and to promote sustainable development. Among the various options for waste heat harvesting, thermoelectric devices that convert heat directly to electricity have shown great potential. Thermoelectric devices are typically composed of pairs of heavily doped n- and p-type semi-conductors that are connected thermally in parallel and electrically in series [1]. The devices contain no mechanically moving parts and thus are noise-free and very stable for long term operation. An individual thermoelectric material is characterized by its dimensionless figure of merit (ZT).

$$ZT = \frac{S^2\sigma}{\kappa}T$$

Where S, σ, κ and T are the Seebeck coefficient, electrical conductivity, thermal conductivity and absolute working temperature, respectively [2]. Considering a thermoelectric device with both n- and p-type materials, the effective ZT is defined by

$$ZT_{eff} = \frac{(S_p - S_n)^2 T}{[(\rho_n \kappa_n)^{\frac{1}{2}} + (\rho_p \kappa_p)^{\frac{1}{2}}]^2}$$

Where ρ is the electrical resistivity, and the subscripts ‘n’ and ‘p’ denote the properties of n- and p-type materials, respectively. The
Effective ZT determines the maximum working efficiency η, by

$$\eta = \frac{T_h - T_c}{T_h}\frac{\sqrt{1 + Z\overline{T}_{eff}} - 1}{\sqrt{1 + Z\overline{T}} + T_c/T_h}$$

T_h, T_c and $\overline{T}$ are the hot side temperature, cold side temperature, and average temperature applied on the thermoelectric device, respectively [2]. Higher ZT is favorable for better device efficiency. To enhance ZT, large Seebeck coefficient and electrical conductivity, as well as low thermal conductivity is desired. There exist various thermoelectric materials for different operating temperatures. A summary of ZT as a function of temperature for state of the art thermoelectric materials is plotted in Fig. 1 [3]. The synthesis methods for those materials are mainly based on powdermetallurgical technologies, like milling, hot pressing or spark plasma sintering. Intensive research was conducted during the last years to enhance ZT and of course substantial progress have been made. For applications between ~400K and 800K PbTe is the traditional material. However, for large scale device applications, PbTe are notorious for the high toxicity of Pb and their weak mechanical strength. The low natural availability of Te [4] and the usage of Te in the photovoltaics hinder the broad application of Te in thermoelectrics. On the other hand skutterudites suffer from poor thermal stability and limited supply of rare-earth elements. Half-Heusler is environmentally friendly, mechnically and thermally robust though cost may be an issue if a lot of Hf is needed. Additionally silicides (p-$MnSi_x$, *n*–$Mg_2Si_{0.4}Sn_{0.6}$) offer a great potential to be used as thermoelectric material due to non-toxicity, low cost and high availability of the starting materials. Furthermore silicides can be produced by using simple and low–cost powder metallurgical methods.

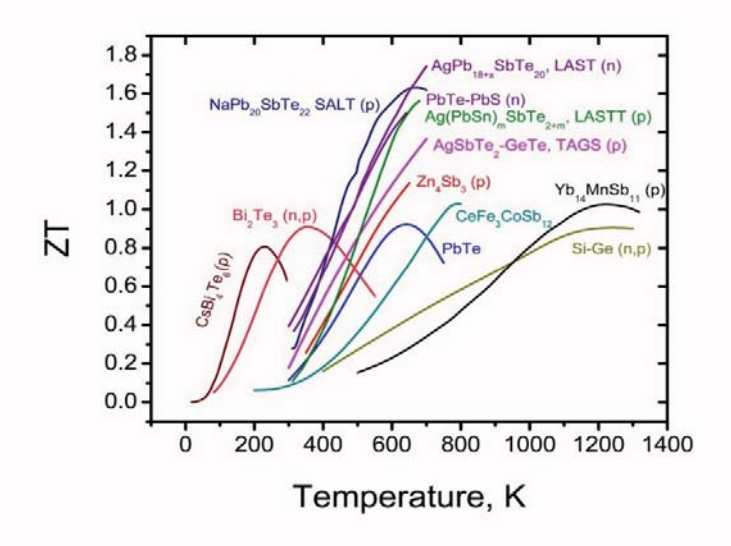

Figure 1. Overview of ZT versus temperature for different thermoelectric materials [3]

EXPERIMENTS

The manganese silicide samples were synthesized by using a powder metallurgical approach. The manganese pieces (Chempur, 99.99 %) and silicon pieces (Silchem, 99.999 %) were first separately ball-milled and later mixed and ball-milled again, in the stoichiometric ratio $MnSi_x$ (X = 1.75, 1.80, 1.85). Both processes were performed under Argon. The manganese pieces were previously cleaned with an aqueous solution of HNO_3 and rinsed with ethanol. The powders were loaded in a graphite die under Ar atmosphere (Ar-Glovebox) reacted and at the same time sintered by Spark Plasma Sintering at 900 °C – 1000 °C, pressure of 50 MPa and 10 min holding time [5].
For the synthesis of magnesium silicides our patented hydride route was used [6]. After high energy milling the powder mixtures were loaded in a graphite die under Ar atmosphere and sintered by spark plasma sintering at 700°C. The temperature profile is characterized by a holding time at 400°C before sintering at 700°C in order to remove the hydrogen formed during the decomposition of MgH_2.

The particle size and size distribution of the milled powders were analyzed with an Ankersmid CIS-100 analyzer using propandiol as dispersive medium. X-Ray powder diffraction analysis were performed at different stages of the synthesis with a Bruker D8 Advance powder diffractometer equipped with a Ge (111) Johansson monochromator and Lynx-eye detector. The density was determined by the Archimedes method in water. Thermal Analysis (DSC-TG) on the sintered materials was performed with a Netzsch STA 449 C Jupiter under Ar with a heating rate of 10 K/min. Scanning electron microscopy characterizations were done with a Zeiss EVO 50 and EDX detector, Si-lithium from oxford instruments. The Seebeck coefficient and the electrical conductivity were simultaneously measured in a ULVAC ZEM3 machine from room temperature up to 700 °C. The accuracy of the measurements was validated by measuring *S* and σ of a Nickel–prism. Our results show an excellent agreement with the published nickel data [8].

RESULTS AND DISCUSSION

Formation of the Mn-Si phases

The final average particle size of the Mn and Si powder (after the first milling process) is very similar for both elements; 10 μm and 12 μm, respectively. The maximal particle size is 30 μm to 40 μm and they represent the 8 % to 10 % of the total amount. For the samples sintered by SPS at 900 °C and 1000 °C a density of 4.9 g/cm^3 and 5.1 g/cm^3 is achieved which represents 95 % and 98 % of the bulk density (5.15 g/cm^3), respectively. The figure 1 shows the XRD patterns of the $MnSi_x$ sintered specimens (x = 1,75 samples (a),(b), 1.80 sample (c) and 1.85 samples (d),(e)). For the samples (a) and (b), with the same nominal composition $MnSi_{1.75}$, it is observed a MnSi secondary phase and for the sample (a) also non reacted silicon. The amount of secondary phase in the sample (b) can be reduced by optimizing the milling/mixing and SPS parameters but it will not completely disappear. The quantity of the MnSi secondary phase can only be further decreased with the increment of the silicon content (x = 1.80 and 1.85), samples (c) (d) and (e). The samples (d) and (e) have the same nominal composition $MnSi_{1.85}$ and their XRD patterns evidence the reproducibility of the results [5].

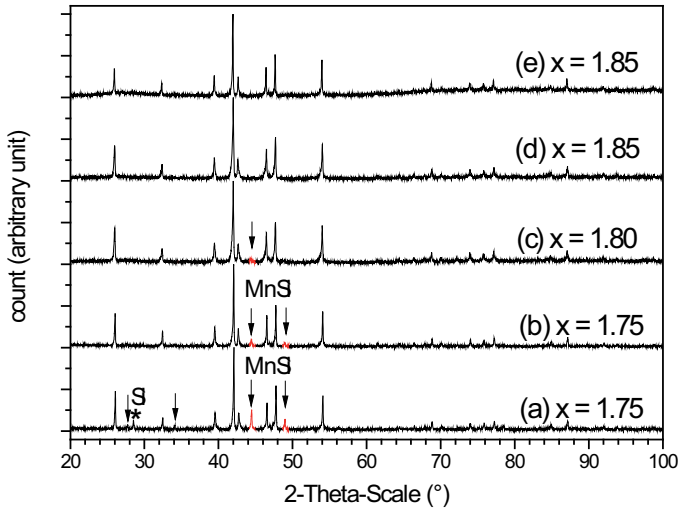

Figure 2. XRD Patterns of $MnSi_x$ samples (x = 1.75, 1.80 and 1.85) sintered at 1000 °C

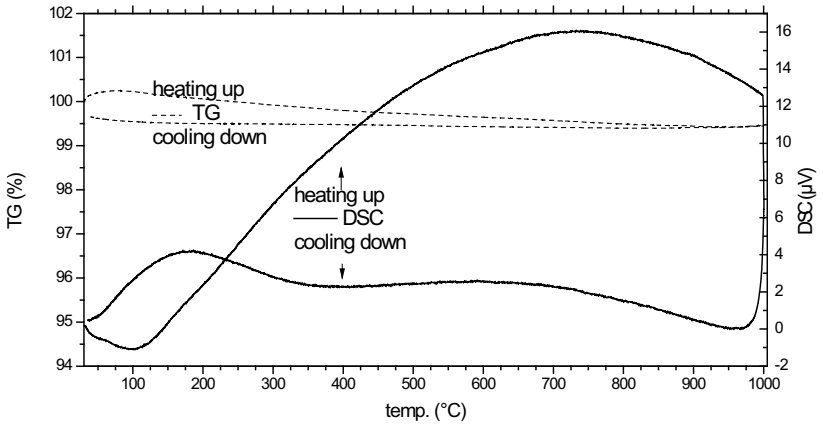

Figure 3. DSC/TG curve of $MnSi_{1.85}$ (d) sample

The figure 2 shows the DSC/TG curve for the $MnSi_{1.85}$ (d) sample from room temperature up to 1000 °C. No thermal effects indicating phase transitions or presence of secondary phases were observed. Changes in the weight of the sample before and after the thermal analysis were not detected (TG-curve). Both results (DSC/TG and metallography) support the observations from the XRD patterns concerning the purity of the sample [5].

Thermoelectric properties

The figure 4 displays the temperature dependence of the Seebeck coefficient. All values are positive and suggest the *p*-type conduction. The sample (a) contains the larger amount of secondary phase MnSi (observed from the relative intensity of the Bragg reflections) and traces of non-reacted silicon. This sample displays the lowest Seebeck coefficient, ~155 μV at 500 °C. As the purity of the sample increases (see figure 2), the Seebeck coefficient rises. The single phase samples (d) and (e) present the largest values ~235 μV at 500 °C which are in agreement with the highest Seebeck values reported in the literature [9]. The high Seebeck values extend over a wide temperature range from ~ 350 °C to 600 °C making their potential applications in the energy harvesting from automobiles very interesting. The figure 5 shows the temperature dependence of the electrical conductivity of the samples with different compositions. The electrical conductivity of the $MnSi_{1.75}$-samples is higher than the rest of the samples because the MnSi-phase is present. As the purity of the samples is improved the electrical conductivity sinks. This indicates that the MnSi phase increases the electrical conductivity. These observations are in agreement with the results from Luo and Umemoto [9, 10]. From figure 5 it is evident that samples (e) and (d), with the same nominal composition, display different electrical conductivity even if both specimens present the same Seebeck coefficient and purity, see figures 2 and 4. This suggests that other factors than sample purity may influence the electrical conductivity, for example the amount of strain and defects density in the sintered body. The figure 6 shows the temperature dependence of the power factor of the $MnSi_x$ samples with different compositions. The $MnSi_{1.85}$ sample (d) shows the largest power factor 0.0015 W/mK^2 at 500 °C and the $MnSi_{1.75}$ sample (a) the lowest value ~ 0.0007 W/mK^2 at 500 °C. Surprisingly, the $MnSi_{1.85}$ sample (e) displays the second lowest power factor ~ 0.0010 W/mK^2 at 500 °C in spite of this sample has the same composition, purity and Seebeck coefficient as the sample (d). This is explained by the low electrical conductivity of (e) in relation to the rest of the specimens. Further investigations are required to explain such behaviour and also to clarify the influence of strain and defects in the electrical conductivity. As observed in the Seebeck coefficient, the high power factor values in sample (b) also extend over a wide temperature range from ~ 350 °C to 600 °C. The characterization of the total thermal conductivity is still in progress. However taking the maximal (~3 W/mK) and minimal (~ 1.7 W/mK) values of thermal conductivity reported in the literature [9-13] we estimate the *ZT* value at 500 °C to be between 0.38 and

0.68. It is very important to outline that these results are obtained in binary samples, that means that further improvement on the thermoelectric properties are expected if the composition of the materials is optimized via doping [5].

Magnesium silicide

Clean preparation conditions and adequate pure reactants (non−oxidized) are crucial for the quality of the final samples. S and σ of are enhanced with the purity of the samples. The temperature dependence of the power factor (*PF*) in single phase $Mg_2Si_{0.4}Sn_{0.6}$ (non−doped) shows two maxima, at ~ 150 °C (5.3 x 10^{-4} W/mK^2) and at ~ 580 °C (4 x 10^{-4} W/mK^2). The temperature dependence of σ reveals the semiconducting character of the specimens. The *PF* of Bi−doped $Mg_2Si_{0.4}Sn_{0.6}$ single phase samples (3.5 x10^{-3} W/mK^2) shows a 10 fold enhancement at 300 °C in relation to the non-doped state which results in $ZT > 1$ (Figure 7). Such an enhancement in the *PF* arises from the large increment of σ due to the doping. The temperature dependence of σ displays the metallic-like character of the doped samples [7].

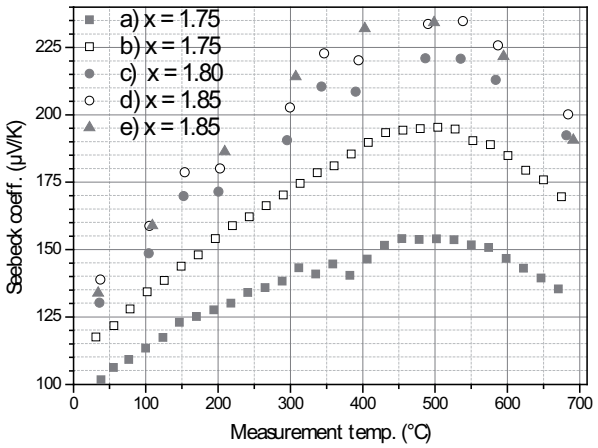

Figure 4. Temperature dependence of the Seebeck coefficient of $MnSi_x$ samples (x = 1.75, 1.80 and 1.85) sintered at 1000 °C

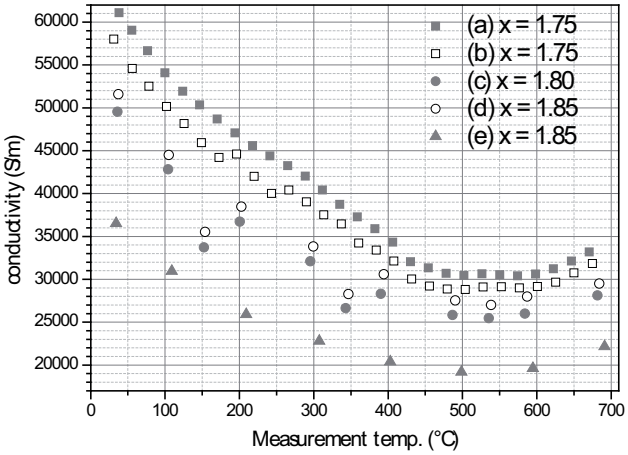

Figure 5. Temperature dependence of the electrical conductivity of $MnSi_x$ samples (x = 1.75, 1.80 and 1.85) sintered at 1000 °C.

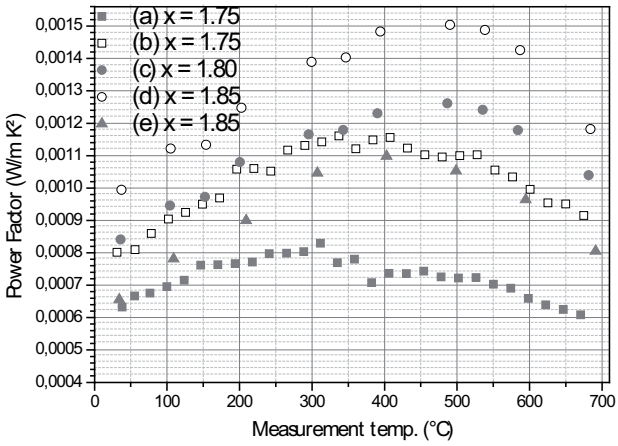

Figure 6. Temperature dependence of the power factor of $MnSi_x$ samples (x = 1.75, 1.80 and 1.85) sintered at 1000 °C.

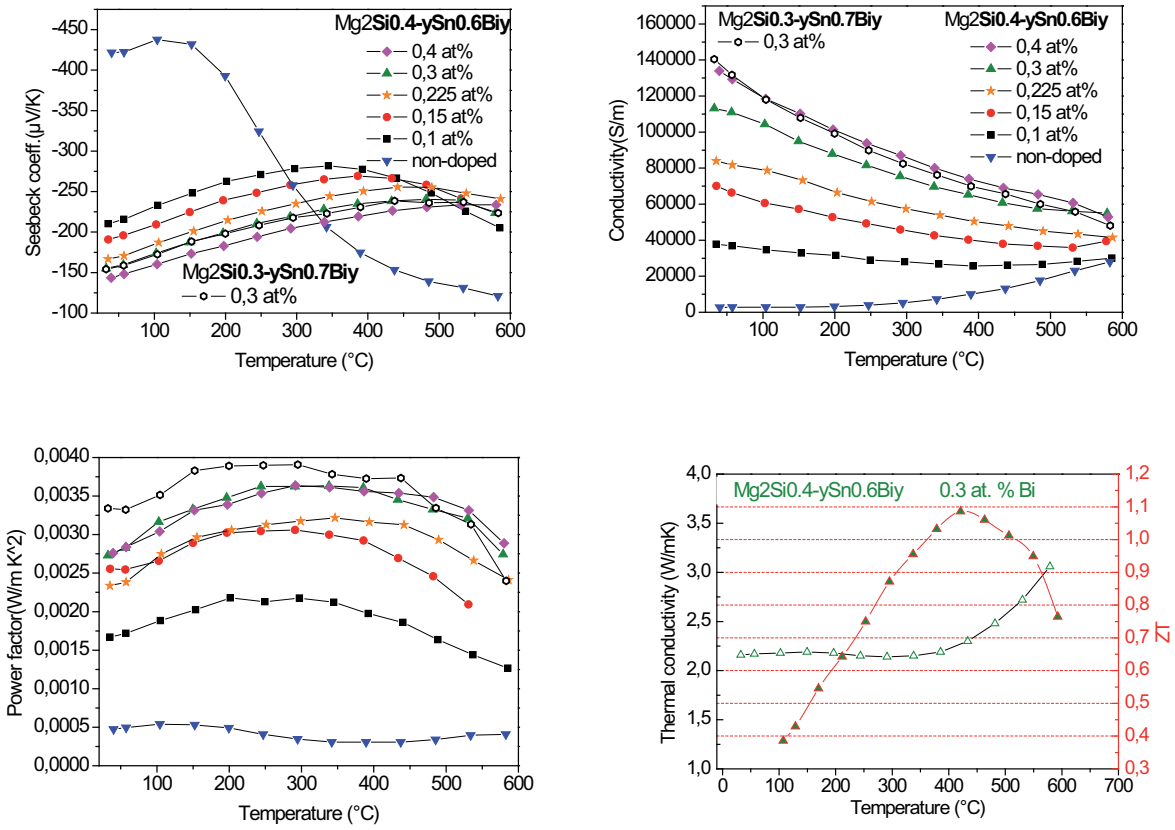

Figure 7. Temperature dependence of the seebeck coefficient, electrical conductivity and power factor as well as ZT value of Bi doped and non-doped Mg-Si-Sn samples

Up-scaling and module manufacturing

The first breakthrough of our research is the production of samples in large scale which preserve the same high quality of the laboratory-scale samples. In first instance, the reaction and sinter parameters of the starting materials were determined in samples of 1 cm in diameter. The results presented in the previous sections were obtained on samples of 2 cm in diameter. The up-scaling for the production of samples with larger diameter is not a trivial task due to the brittle character of the silicides. With a further optimization of the SPS parameters and the development of adequate graphite pressing tools we succeed in the preparation of sinter materials with a diameter of 6.0 cm. To our knowledge these are the largest silicides wafers produced up to now. The sintered discs are mechanical stable to allow their polishing to a mirror surface (figure 8) and the sectioning into thermoelectric legs. The pre-contacting and subsequent soldering is essential to produce TE-modules. Sintered discs of silicides were first produced and then polished to obtain parallel faces. The polished sinter bodies covered with a metal foil were loaded in the graphite die and pre-contacted via SPS. This technology opens the possibility of producing pre-contacted thermoelectric legs at large scale.

Applying the developed pre-contacting and soldering technology modules with up to 10 legs can be manufactured (Figure 9).

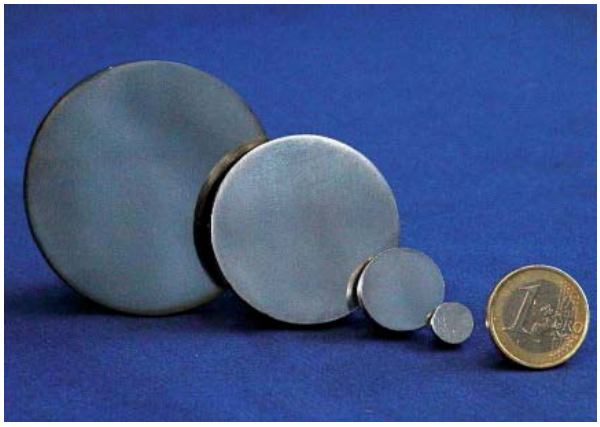

Figure 8. Sintered discs of Mg-silicides with diameter of up to 6.0 cm

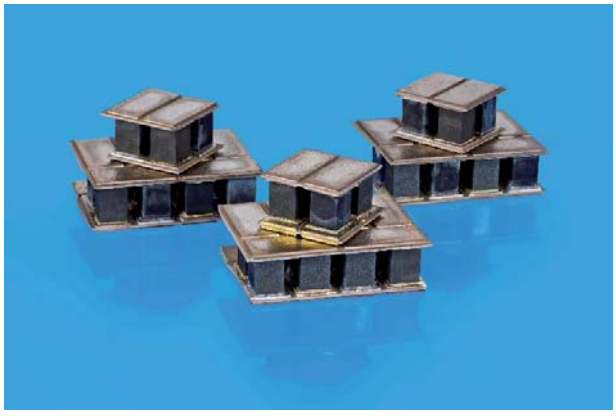

Figure 9. Thermoelectric Modules based on silicide materials

SUPERCAPACITORS

PM Technology to manufacture supercapacitors

To store the generated power supercapacitors with high power and energy density could be an attractive solution. Supercapacitors are a class of electrochemical energy-storage device that could complement batteries for load-leveling or uninterruptible power supply applications [14]. In terms of their specific energy and specific power, they fill the gap between conventional capacitors and batteries (Figure 10 [19]). These devices can be included in a hybrid configuration to manage short, high power pulses, thereby minimizing stresses on the primary energy storage device. Currently available supercapacitors are very well suited to handle pulses of up to a few seconds [19]. To achieve broader application, capacitors will have to efficiently manage longer pulses which translates to higher energy densities. Conventional supercapacitors store energy via the formation of an electrical double-layer at the electrode/electrolyte interface [14]. Most commercial supercapacitors use very high-surface-area carbon-based materials. These materials yield specific capacitances in the range of 100 F/g and energy densities up to 5Wh/kg for corresponding devices [15, 16]. Some materials exploit fast, reversible faradaic redox reactions that occur within the first few nanometers of the surface of the active materials [19]. This pseudocapacitve mechanism has been demonstrated for materials including metal oxides and hydroxides. Hydrous RuO_2 is a benchmark pseudocapacitive material and has been shown to yield specific capacitances ranging from 720-1300 F/g depending on the preparation and heat treatment conditions [17, 18]. Despite the high specific capacitance of the ruthenia based materials, their high cost makes them unattractive for large-scale use and therefore the commercial application of Ru-based supercapacitors has been limited. Recently, early transition metal nitride-based materials have been reported to exhibit pseudocapacitive behavior [20-28]. These materials have electronic conductivities that are much higher than those for transition-metal oxides, and can be produced with surface areas exceeding 100 m^2/g [29] and specific capacitances >200F/g [30].
The overall goals are to design and construct a high power, high energy density prototype supercapacitor based on metal foams and nanostructured early transition metal carbides and nitrides.

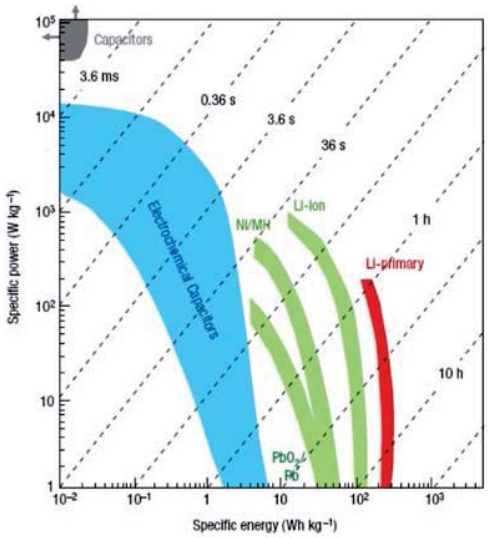

Figure 10. Plot of specific power against specific energy, also called Ragone Plot, for various electrical energy storage devices. Times shown are the time constants of the devices, obtained by dividing the energy density by the power. Figure taken from reference [19].

Alloy Foam Production and Infiltration

Technology for production of the metallic foams was developed in a collaboration between ALANTUM Corp. and Fraunhofer IFAM for mainly diesel particle filter and catalyst carrier applications. This process will be now used and further developed to produce foams for use as electrodes and active material carriers for new high performance supercapacitor. The 3D structure of the current collector offers following advantages compared to foils:

- Three-dimensional metal foam structure results in excellent electical contacting between electrodes and active materials, which reduce the inner resistance and increase the power density
- Good heat conductivity and heat distribution
- Remaining pores after infiltration of active material achievable by electrolyte
- Easy to infiltrate by active materials
- High surface area available
- Geometry and shape can be adjusted for each canning design
- Commercial production for customer tailored solutions available
- High design flexibility and workability
- Foam alloy is adjustable for the respective application and operation conditions (e.g. corrosive electrolytes or interactions with active materials)

Figure 11 shows a schematic of the patented manufacturing process [31-36] to transform the commercially available Ni foam into an alloyed foam with high oxidation and corrosion resistance. The main features of this powder metallurgical process are the coating of the Ni foam with a binder using a spraying process and afterwards with a specified high alloyed metal powder. The subsequent heat treatment includes debindering and sintering steps (see Figure 12). During the transient liquid phase sintering process, elements from the powder diffuse rapidly into the foam struts and ensure a homogeneous alloy foam composition. Micrographs in Figure 13 compare the pure Ni foam and the alloyed foam. The high roughness of the alloyed foam offers a number of advantages, including high specific surface area and good adhesion of coatings that will be described in the sections to follow. Two of the basic foam properties, namely surface area and volumetric density as well as the foam sheet thickness, are summarized in Table I for the commercially available pore sizes.

The alloy foam material is to act as current collector and carrier for the active material which is storing the electric energy. The experimental work was started using vanadium nitride as active material and Inconel 625 foam to prepare electrode material. During the experimental work two different processing routes were carried out to integrate the active material in the three dimensional structure of the metal foam. Depending on the used powder (oxide or nitride) the sequence of the processing steps is different:

Variant 1: V_2O_5 powder infiltration into IN 625 foam→nitride synthesis of infiltrated foam by temperature programmed reaction (TPR)

Variant 2: synthesis of VN powder from V_2O_5 (TPR) →infiltration of powder slurry into IN 625 foam

The process starts with the infiltration of a powder slurry consisting of a binder solution and a transient metal based powder (transient metal oxide powder or carbides/nitrides from transient metal powder corresponding to variant 1-2) into the foam by a doctor blade. The challenge was to achieve a high powder loading in the foam. Generally the full infiltration without remaining bubbles is easier for the foam with a pore size of 1200 µm foam compared to a 450 µm foam. However, the 450 µm foam with its more filigree strut network is preferred with regard to conduction contacts with the active material and improving the power density. To increase the contact between the foam electrode and the active material as well as to remove remaining bubbles the foam was calendared. Figure 14 shows an example for infiltrated electrode materials. Up to 79 wt% powder filling ratio was achieved which correlates to a nearly complete infiltration of the pore volume of the foam. Afterwards a drying process follows.

The correlation between the active powder loading value and the obtainable energy densities are drawn in Figure 15. In the upper curve the energy density using ready VN powder (transformed from V_2O_5 to VN separately before infiltration) is given. The lower curve demonstrates the energy densities using V_2O_5 powder for infiltration with an enclosed synthesis to VN. The lower energy densities for the same filling

ratio are the result of weight loss during the reaction from V_2O_5 to VN by a factor 0,714. The range of possible powder loading depends on one hand on the powder slurry composition (amount of solvent and binder) and on the other hand on the foam morphology. The foam with a pore size of 1200 µm has a lower strut density and can absorb more powder slurry compared to a 450 µm foam. On the other side a higher

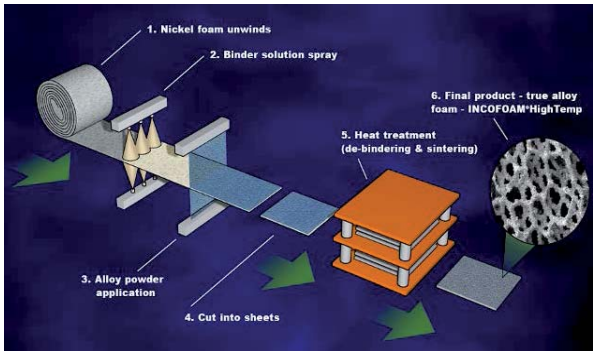

Figure 11 Manufacturing process for alloyed Ni based foam (schematic).

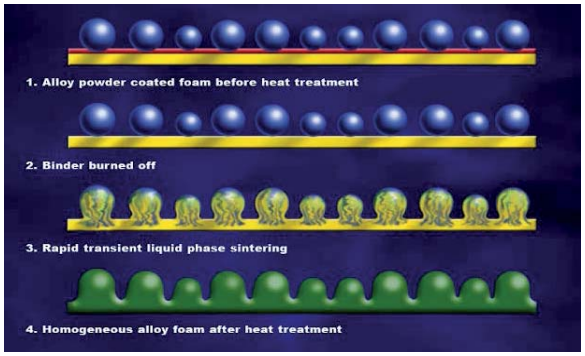

Figure 12 Schematic illustration of processes occurring during transient liquid phase sintering with increasing temperature and time.

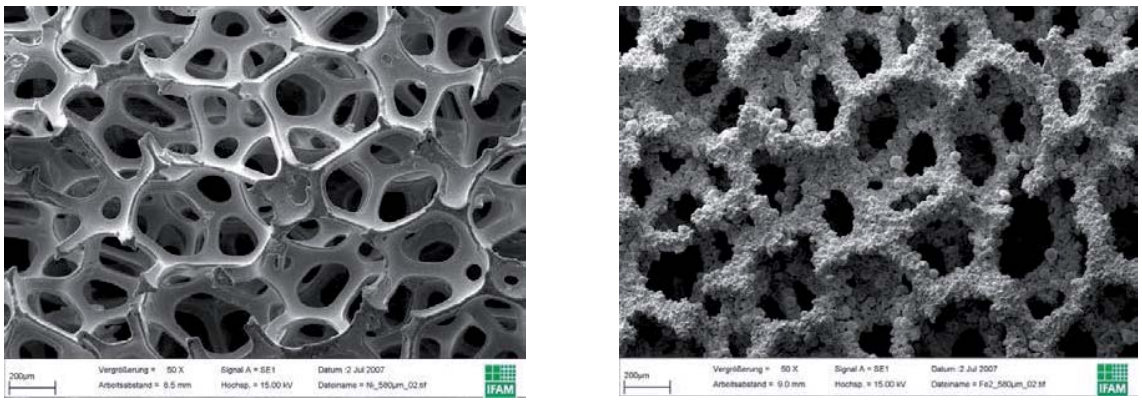

Figure 13 Scanning electron micrograph of pure Ni (left) and alloyed (right) foams.

strut density can bear higher currents. The general level of the energy density (which is > 10 Wh/kg for the obtained powder loadings) of the electrode material is promising to achieve higher performance compared to state of the art super capacitors.

Table I Summary of foam density and thickness for the available pore sizes.

Pore size [µm]	alloyed foam		
	density (g/m^2)	density (g/cm^3)	thickness (mm)
450	1150	0,72	1,60
580	1150	0,60	1,90
800	1195	0,48	2,50
1200	1235	0,41	3,00

a) 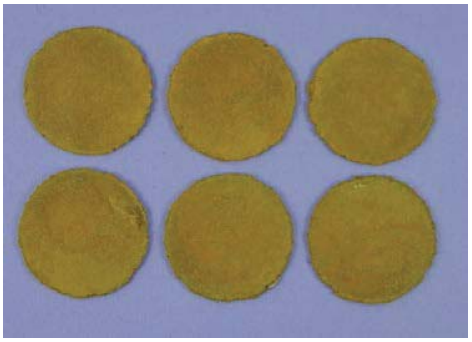 b) 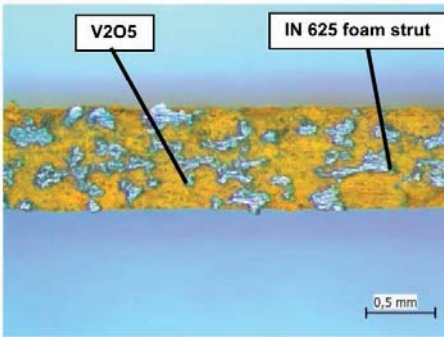

Figure 14. With V_2O_5-powder slurry infiltrated foam disks of 16 mm diameter for button cell test before nitride syntheses (450 µm foam, IN625) after 50% calendaring (Filling ratio V_2O_5: 79 wt %; a) disk samples;
b) cross section of the disk samples with fully infiltration of the foam volume)

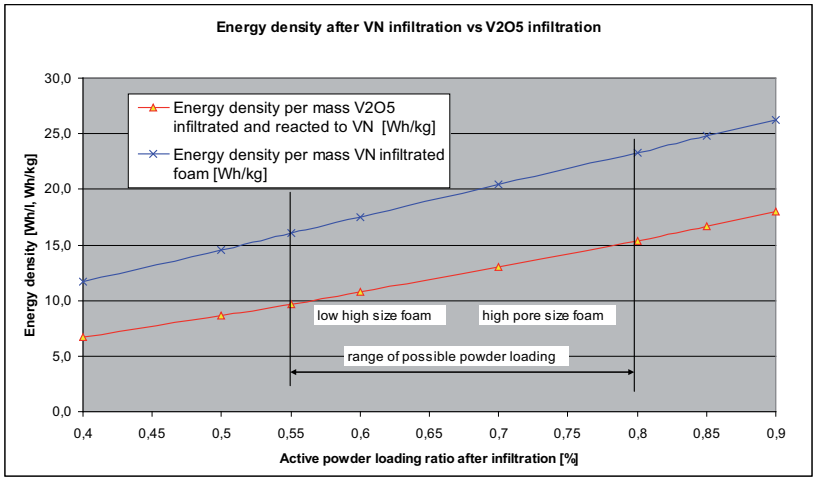

Figure 15. Correlation between the active powder loading value and the obtainable energy densities for complete electrodes (upper curve for using VN powder, lower curve for using V_2O_5 powder with synthesis to VN after infiltration)

Supercapacitor Prototypes

The pure alloy foam has a high degree of design flexibility. It can be cut, shaped by rolling, pressing or calendering. After infiltration of the pore volume and drying the shaping properties are limited. On the other hand, powder infiltration after shaping would be very difficult or impossible. One option would be the shaping of the infiltrated electrode material in wet state. Most promising is a design based on flat sheets, which can be folded as electrodes into one another insulated with the separating foil (see Fig. 16). The advantage of such a design is that no additional conducting of several layers is needed. Only the two ends of the electrodes have to be connected. To improve the bendability notches can be pressed in the foam. The compressed areas have a thickness of about 100 µm, like a flexible foil. The areas between the pressed sections will be infiltrated with the active material. Afterwards the electrode will be bent along the pressed lines and the two electrodes can be separated by an insulating porous polymer film wetted with electrolyte. All the parts will be assembled. Calculations of the energy density have shown that values of about 10Wh/kg are feasible. This is a promising value and shows the high potential of this concept, because the energy densities of state of the art supercapacitors is < 5 Wh/kg.

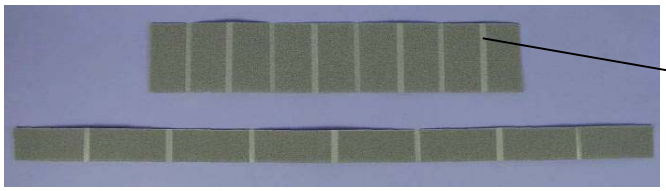

a)

b)

- Cutting IN625 foam strips (2 electrodes)
- Pressing lines for bending
- Infiltration with active material
- Assembly of electrodes with seperator wetted with electrolyte
- Conducting electrodes
- Canning

Figure 16. Supercap design study, a) foam electrode to be infiltrated, b) folded electrodes with separator and canning (canning size 45 mm x 25 mm x 15 mm)

CONCLUSION

The presented results on the synthesis, thermoelectric properties and production up−scaling of *p*–$MnSi_x$ ($1.75 \leq x \leq 1.85$) and *n*–$Mg_2Si_{0.4}Sn_{0.6}$ have shown the potential of such material for energy harvesting at elevated temperatures. The paper presented promising ZT values by optimizing the chemical composition as well as the manufacturing technology. Further enhancement in the PF and *ZT* will obtained by doping, which is in the focus of further work. Aspects related to the oxidation of the silicides will also addressed in the future.

The results on supercapacitors indicate a high potential of the new material concept for high power and energy density supercapacitors. The work will continue for increasing the electrode and test cell performance, the optimizing the syntheses conditions for a further increase of the specific surface of the active material as well as the cell design with their components like electrolyte, separator and conducting of current collectors.

REFERENCES

[1] Snyder GJ, Toberer ES. Complex thermoelectric materials. Nature Materials 2008;7:105.
[2] H.J. Goldsmid, D.M. Rowe (Ed.), Conversion Efficiency and Figure-of-Merit, CRC Handbook of Thermoelectrics, Boca Raton
[3] http://chemgroups.northwestern.edu/kanatzidis/greatthermo.html
[4] R. Amatya, R.T. Ram. Journal of electronic materials, Vol. 41, No. 6, 2012
[5] V. Pacheco, C. Recknagel, H. Görlitz, T. Weißgärber, B. Kieback. 3rd IAV Tagung Thermoelektrik, 21.-23. November 2012, Berlin, Germany
[6] Patent EP 1 409 407 B1
[7] V. Pacheco, C. Recknagel, G. Pöhle, F. Senftleben, S. Wieland, T. Weißgärber, B. Kieback. 11th European Conference on Thermoelectrics, 18.-20. November 2013, Noordwijk, Netherlands
[8] A.T. Burkov, A. Heinrich, P.P. Konstantinov, T. Nakama and K. Yagasaki. Measurement Science and Technology 12, 264 – 272, 2001
[9] M. Umemoto, Z.G. Liu, R. Omatsuzawa and K. Tsuchiya. Materials Science Forum Vols. 343-346, pp 918-923, 2000
[10] W. Luo, H. Li, Y. Yan, Z. Lin, X. Tang, Q. Zhang, C. Uher. Intermetallics 19, 404-408, 2011
[11] A. J. Zhou, X.B. Zhao. T.J. Zhu, Y.Q. Cao, C. Stiewe, R. Hassdorf and E. Mueller. Journal of Electronic Materials, Vol. 38, No 7, 2009
[12] Y. Sadia and Y. Gelbstein. Journal of Electronic Materials, Vol. 41, No 6, 2012
[13] W. Luo, H. Li, F. Fu, W. Hao nd X. Tang. Journal of Electronic Materials, Vol. 40, No 5, 2011
[14] Burke, Andrew; Electrochimica Acta 53, (2007) 1083.
[15] P. Simon, A. Burke, The Electrochemical Society: Interface Spring, 2008, p. 38.
[16] A. Burke, Int. J. Energy Res. 34 (2010) 133.
[17] Zheng, J.P., P.J. Cygan, and T.R. Jow, J. Electrochem. Soc., 1995. 142(8): p. 2699-703.
[18] Hu, C.-C., et al., Nano Lett., 2006. 6(12): p. 2690-2695.
[19] Simon, Patrice; Gogotsi, Yury; Nature Materials 7, (2008) 845.
[20] Choi, D. and P.N. Kumta, Solid-State Lett., 2005. 8(8): p. A418-A422.
[21] Choi, D., G.E. Blomgren, and P.N. Kumta, Adv. Mater. (Weinheim, Ger.), 2006. 18(9): p. 1178-1182.
[25] Zhou, X., et al., J. Phys. Chem. Solids, 2009. 70(2): p. 495-500.
[26] Glushenkov, A.M., et al., Chem. Mater.: p. ACS ASAP.
[27] Liu, T.C., et al., J. Electrochem. Soc., 1998. 145(6): p. 1882-1888.
[28] Choi, D. and P.N. Kumta, J. Am. Ceram. Soc., 2007. 90(10): p. 3113-3120.
[29] Wixom, M. R.; Tarnowski, D. J.; Parker, J.M.; Lee, J. Q.; Chen, P-L; Song, I.; Tompson, L.T.; Material Reasearch Society Symposium Proceedings 496 (1998) 643.
[30] P Pande, P. G. Rasmussen, L. T. Thompson, Charge storage on nanostructured early transition metal nitrides and carbides, Journal of Power Sources 207 (2012) 212– 215
[31] A. Böhm, H. Goehler, D. Naumann. German patent, DE 101 50 948 C1, 2003
[32] G. Walther, A. Böhm, Th. Weißgärber, H.-D. Böhm, B. Engelmann, D. Naumann. German patent, DE 103 16 929 B3, 2005, European patent EP 1 620 370 B1, 2006
[33] A. Böhm, G. Walther, D. Naumann, L. Timberg. German patent, DE 10 2004 014 076 B3, 2005

[34] A. Böhm, G. Walther, D. Naumann. German Patent, DE 103 46 281 B4, 2006, World Patent, WO 2005/037467 A2, 2005
[35] A. Böhm, G. Walther, D. Naumann, L. Timberg. German patent, DE 10 2005 010 248 B4, 2006
[36] A. Böhm, G. Walther, D. Naumann. German patent, DE 10 2004 032 089 B3, 2005